Nanoscale

PAPER

Cite this: *Nanoscale*, 2024, **16**, 6669

Inhibition of ion diffusion/migration in perovskite p–n homojunction by polyetheramine insert layer to enhance stability of perovskite solar cells with p–n homojunction structure†

Dong Wei, *‡[a] Qingrui Cai,‡[a] Shidong Cai,[a] Yongjing Wu,[a] Mingliang Wang,[a] Peng Cui,*[b] Jun Ji,*[c] Zhirong Zhang,[d] Luyao Yan,[b] Jiahuang Zhang,[a] Jiaqi Luo,[a] Xiaodan Li [e] and Meicheng Li *[b]

Received 16th August 2023,
Accepted 4th March 2024

DOI: 10.1039/d3nr04117d

rsc.li/nanoscale

Perovskite p–n homojunctions (PHJ) have been confirmed to play a crucial role in facilitating carrier separation/extraction in the perovskite absorption layer and provide an additional built-in potential, which benefits the inhibition of carrier recombination in perovskite solar cells (PSCs) and ultimately improves device performance. However, the diffusion and migration of ions between n-type and p-type perovskite films, particularly under operational and heating conditions, lead to the degradation of PHJ structures and limit the long-term stability of PSCs with PHJ structure (denoted as PHJ–PSCs). In this study, we propose an insert layer strategy by directly introducing an ultra-thin polyetheramine (PEA) layer between the n-type and p-type perovskite films to address those challenges arising from ion movements. Femtosecond transient absorption (fs-TAS) and photoluminescence (PL) measurements demonstrate that the PHJ (without and with the insert layer) enhances carrier separation/extraction compared to the single n-type perovskite film. Monitoring the evolution of bromine element distribution reveals that the insert layer can efficiently suppress ion diffusion between perovskite films, even under long-term illumination and heating conditions. Consequently, an efficiency of 23.53% with excellent long-term operational stability is achieved in the optimized PHJ–PSC with the insert layer.

1. Introduction

Organic–inorganic hybrid perovskite solar cells (PSCs) have received much attention in the past decade owing to their ceaseless breakthroughs in power conversion efficiencies (PCEs); therefore, they are regarded as promising candidates for next-generation photovoltaic technologies.[1–7] Throughout the development of PSCs in recent years, it has become obvious that the rocket-like improvement of PCE is mainly related to the suppression of carrier recombination in devices.[8–13] To promote the transport efficiency of photo-generated carriers and lessen the undesired non-radiative recombination, various efficient modification methods, such as passivation strategy, 2D/3D interface engineering and energy band alignment strategy, have been developed.[14–20] Moreover, ingenious structural design, such as bulk heterojunction structure, perovskite–perovskite tandem structure and graded perovskite homojunction structure, have been certified to be valid for inhibiting carrier recombination in PSCs.[21–27] Therefore, the utilization of modification materials and innovative structures are beneficial to suppress carrier losses and enable a PCE closer to the theoretical value.

Benefiting from the self-doping property of perovskite materials, the conducting type of as-prepared perovskite films could be regulated facilely between n type and p type just by adjusting the perovskite component and annealing process.[28–30] This makes it possible to construct PSCs with p–n homojunction structure similar to those of the highly efficient crystalline silicon (c-Si) solar cells. In 2019, the perovskite p–n homojunction (PHJ) was constructed successfully for the first time, which can orient the carrier transport and suppress carrier recombination by the built-in electric field produced from the PHJ structure.[31] By introducing PHJ into PSCs, the

[a]*College of Physics and Energy, Fujian Normal University, Fuzhou, 350117, P. R. China. E-mail: q397983012@126.com*
[b]*School of New Energy, North China Electric Power University, Beijing, 102206, P. R. China. E-mail: cuipengmvp@163.com, mcli@ncepu.edu.cn*
[c]*Beijing Huairou Laboratory, Beijing 101400, P. R. China. E-mail: jijun@hrl.ac.cn*
[d]*Institute of New Energy, HeXi University, Zhangye, 734000, P. R. China*
[e]*Xiamen Univ. Technol., Sch. Mat. Sci. & Engn., Fujian Prov. Key Lab Funct. Mat. & Applicat., Xiamen, 361024, P. R. China*
†Electronic supplementary information (ESI) available. See DOI: https://doi.org/10.1039/d3nr04117d
‡These authors contributed equally.

efficiency increased dramatically from 20.88% to 21.88%, and the carrier recombination rate decreased obviously in the perovskite absorption layer, as reported in the published study. Although the PHJ–PSCs exhibit striking improvement of efficiency and attractive application potential, the long-term stability issues of PHJ structure have impeded its development towards mass production.

As the p-type and n-type perovskite films in PHJ structure contact directly, ions with different concentrations in the two layers tend to spontaneously diffuse into each other, changing the composition of p-type and n-type films, especially under operation conditions. This can easily lead to the damage of PHJ structure after a period of operation, thus accelerating the degradation of PSCs. Hence, it is critical to inhibit the diffusion and migration of ions in the PHJ structure to overcome the stability issues under long-term operation conditions. Ji *et al*. introduced phenethylammonium iodide (PEAI) into the n-type perovskite film to inhibit the doping defect diffusion in the PHJ structure.[32] They confirmed that molecular PEAI can block the vacancy transition channel of interstitial methylamine and bind iodine atoms through hydrogen bonds, which increases the active energy of ion diffusion. Thus, PSCs with PEAI-modified PHJ structure exhibited more stable performance compared with control devices, maintaining 75% of their initial PCE after an 80 °C aging process for 240 h. The bismuth insert layer was also employed to block the diffusion of iodide ions in the perovskite/metal interface. The thin and compact bismuth interlayer not only can protect perovskite film from being corroded by external moisture but also protect the metal electrode from iodine corrosion. Thus, the unencapsulated device with bismuth interlayer exhibited much stable performance.[33] In addition, organic materials with functional groups, such as cellulose, *n*-hexyl trimethyl ammonium bromide (HTAB) and gallium(III) bromine, were utilized as the insert layer to enhance the stability of PSCs.[34–36] Despite the clear improvement, questions regarding the inhibition of ion diffusion for enhancing the stability of PHJ–PSCs are still open.

In this study, we adopted the insert layer strategy to enhance the stability of PHJ structure and corresponding PSCs. By introducing an ultra-thin PEA layer between the n-type and p-type perovskite films, the PHJ with an insert layer could be fabricated successfully. The PEA insert layer efficiently suppresses the diffusion and migration of ions between the n-type and p-type perovskite films under heating and light-exposure conditions. The efficiency of PHJ–PSCs with the insert layer exhibits an obvious improvement, up to 23.53% compared with that of traditional planar PSCs (20.92%). The unencapsulated PHJ–PSCs with the insert layer demonstrate outstanding stability, maintaining their initial efficiency of over 80% for 500 hours under one-sun illumination and MPP tracking. This study highlights a facile way to enhance the stability of PHJ structure, which is beneficial for the future commercialization of PHJ–PSCs.

2. Results and discussion

The process of fabricating the PHJ is shown in Scheme 1. Initially, the n-type perovskite film is directly deposited on the FTO/TiO_2 substrate through the spin-coating method. During the spin-coating process, one milliliter of diethyl ether, as the antisolvent, was dripped onto the surface of the perovskite film. Then, the wet film was annealed at 150 °C for 15 minutes to obtain a black perovskite film. Subsequently, the diluted PEA solution (diluted with IPA) was spin-coated onto the n-type perovskite film, followed by the fabrication of a 300 nm PbI_2 film (Fig. S1†) on the PEA layer using the vacuum evaporation method. The employed PEA had an average molecular weight of approximately 230 Da, and its molecular structure is depicted in Fig. S2.† Finally, the FAI solution was spin-coated onto the PbI_2 film, and the p-type perovskite film was formed

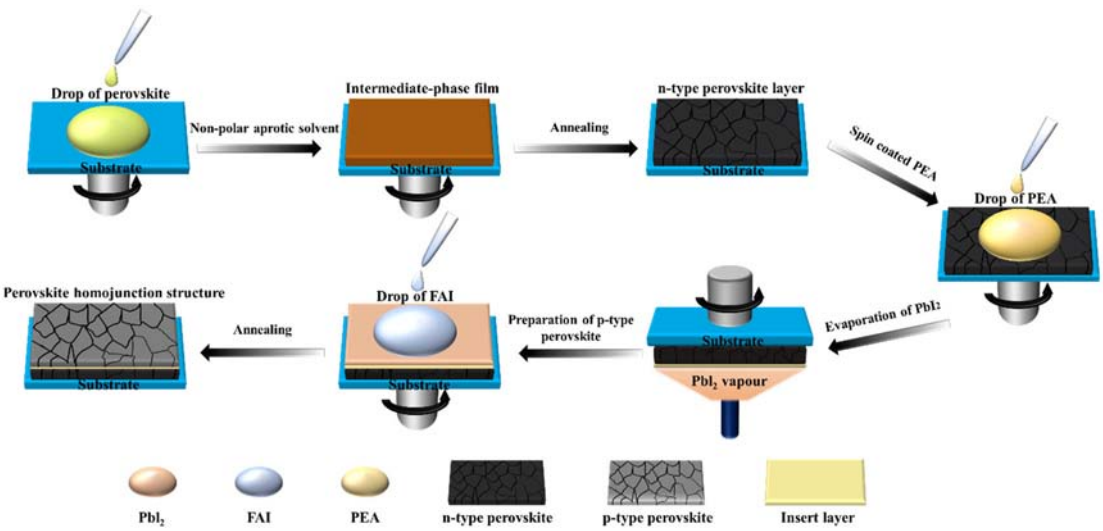

Scheme 1 Fabrication process of the PHJ with PEA insert layer.

after the annealing process. In the Experimental section, a more detailed description of the fabrication process can be found. The formation of n-type and p-type conductive perovskites is attributed to deviations from the ideal stoichiometry during the preparation of the perovskite films, which lead to the emergence of defects and consequent self-doping phenomena within the perovskite structure. When the perovskite film exhibits a Pb-rich/I-deficient condition, donor defects are introduced, thereby giving rise to n-type doping in the perovskite film. Conversely, when the film exists in a MA-rich/Pb-deficient state, acceptor defects occur, resulting in the development of p-type doped perovskite layers.[37,38]

To investigate the effect of the insert layer on the morphology and structure of the perovskite homojunction, we used scanning electron microscopy (SEM) to characterize the surface and cross-sectional morphology of the films. The cross-sectional images inset in Fig. 1a and b confirm that the fabrication process described in Scheme 1 successfully constructed the perovskite homojunction structures, without and with an insert layer. The n-type and p-type perovskite film thicknesses were 500 nm and 400 nm, respectively. For the insertion layer, a thickness of 10 nm was optimized based on the performance of fabricated devices. Moreover, as shown in Fig. S3,† we utilized SEM coupled with EDS analysis to verify the presence of the PEA insertion layer. Top-view images show that the surface morphology of the perovskite homojunction with the PEA insert layer is more compact and uniform compared to that without the insert layer. In addition, the roughness of upper perovskite films (p-type layer) without and with PEA confirmed that the PEA insert layer reduces the roughness of the upper perovskite film, resulting in a more compact and smoother perovskite film as shown in Fig. 1d and e. The average grain size of perovskite thin films increased from 350 nm without PEA addition to 800 nm upon the inclusion of PEA, suggesting that the PEA layer promotes perovskite grain growth. To understand this phenomenon, contact angle measurements were conducted, as depicted in Fig. S4.† The PEA layer exhibited a contact angle of 76.2°, significantly higher than the 63.3° observed for the perovskite film. The increased contact angle following spin-coating of the PEA insertion layer implies a reduction in nucleation sites, thereby preventing mutual collisions among grains during the growth process that can lead to premature termination due to overcrowding, thus preserving grain size.[39–41] Furthermore, comparative contact angle tests were performed on samples with and without PEA insertion layers, featuring device structures of n-type perovskite film/PbI_2 (PEA-free) and n-type perovskite film/PEA/PbI_2 (with PEA). As shown in Fig. S5,† the sample containing PEA displayed a contact angle of 73.8°, distinctly higher than the 60.7° for the sample without PEA. Consequently, the PEA insertion layer still impacts the wettability of the overlying PbI_2 layer, thereby influencing the growth behavior of p-type perovskite thin films. As shown in Fig. 1c, X-ray diffraction (XRD) patterns reveal the crystalline structures of various film samples. In n-type perovskite films, the n-type perovskite film covered with the PEA layer and the p-type perovskite film on the PEA layer, corresponding crystal planes exhibit distinct diffraction peaks at specific 2θ values indicative of cubic phase perovskite. Notably, extremely intense diffraction peaks are observed for the (001) and (002) crystal planes of the perovskites, suggesting that these perovskite films uniformly possess a high degree of crystallographic orientation and exhibit a highly crystalline quality in their cubic phase.[42–44] Furthermore, as depicted in Fig. 1c, pristine perovskite film samples exhibit PbI_2 diffraction peaks, suggesting the presence of residual PbI_2 within the film matrix. During the device fabrication process, a PEAI passivation layer was spin-coated on the surface of the upper perovskite film for all devices. As shown in Fig. S6,† upon application of the PEAI passivation treatment, the intensity of PbI_2 diffraction peaks significantly decreases in the n- and p-type perovskite films, indicating that the PEAI passivation layer effectively reduces the residual PbI_2 content in the perovskite films. This reduction minimizes the impact of PbI_2 on carrier transport in the perovskite homojunctions.

To determine the conductive type of the bottom and upper perovskite films, Kelvin probe force microscopy (KPFM) and ultraviolet photoelectron spectroscopy (UPS) were also employed, as shown in Fig. 1f–k. On comparing mapping images shown in Fig. 1f and g, it is evident that the contact potential difference (CPD) of the as-prepared n- and p-type perovskite films display notable differences. Three linear sections were selected from CPD images to estimate the average values of these films, and corresponding CPD profiles are displayed in Fig. 1h and i. Then, the work functions of these films can be calculated by eqn (1):

$$\varphi_s = \varphi_t - eV_{sp}, \quad (1)$$

where φ_t is the work function of Au, e is the elementary charge, and V_{sp} is the value of CPD. The work function of the n-type perovskite was measured to be −4.31 eV and that of the p-type perovskite was found to be −5.44 eV. The lower the work function, the closer the Fermi level is to the vacuum level, indicating that the perovskite film has n-type conductivity, whereas a higher work function suggests that the Fermi level is closer to the valence level, indicating p-type conductivity. In addition, dark current measurements were performed on devices with a structure of FTO/TiO_2/perovskite film/Au, as depicted in Fig. S7.† In the single-layer perovskite configuration, minimum dark current shifts towards negative bias voltages, whereas in devices incorporating homojunction perovskite films, the minimum dark current is observed to shift towards positive biases. This observation suggests that the introduction of the homojunction structure leads to a transition from a potential dominated by ion accumulation at interfaces to one governed by the built-in potential within the homojunction itself. Furthermore, UPS characterization was performed to gather more precise information about the energy levels of the perovskite films. The Fermi and valence levels of the n- and p-type perovskite films were determined by fitting the profiles in Fig. 1j and k, respectively. Therefore, it

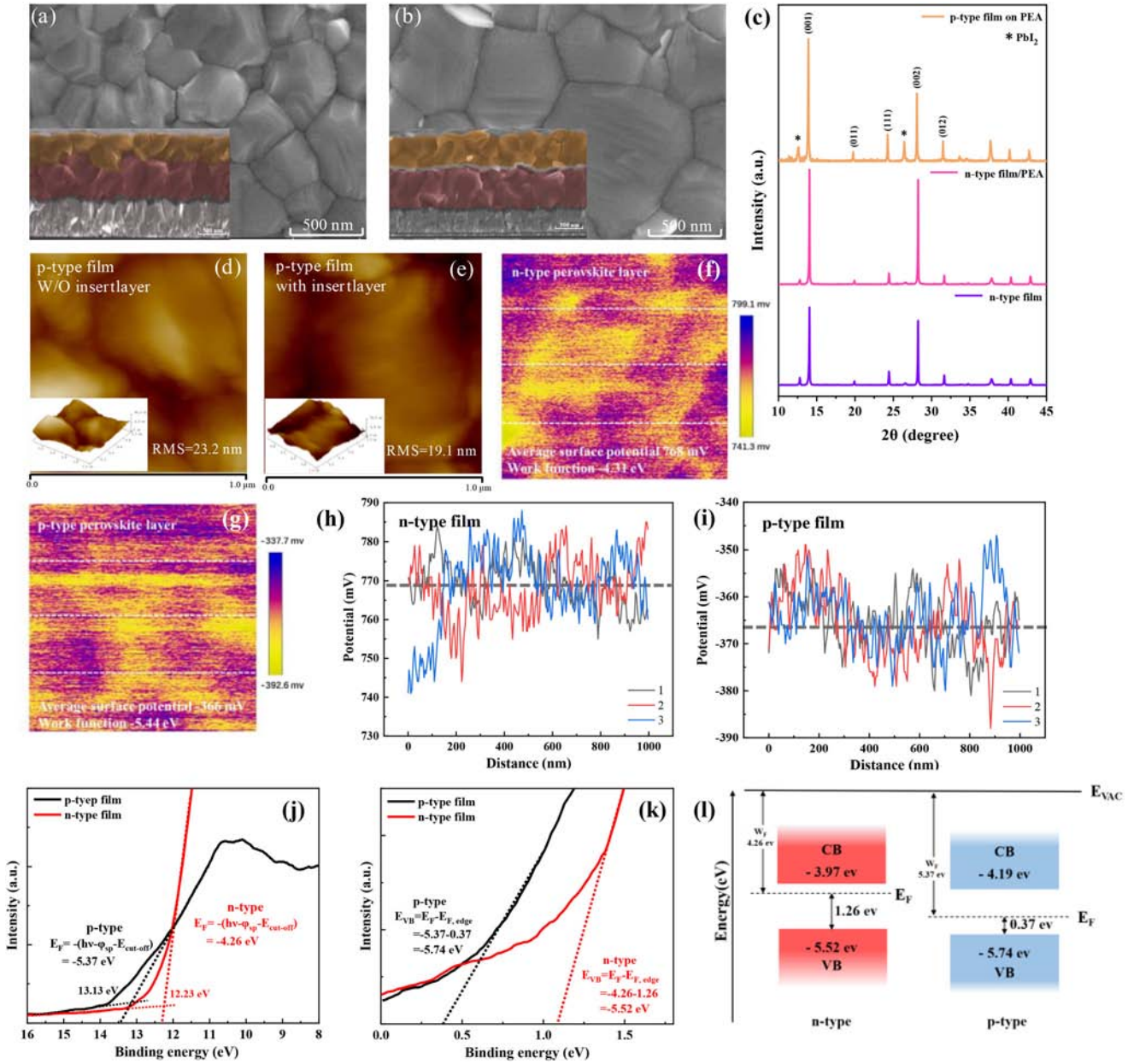

Fig. 1 Structural and conduction-type characterization of the perovskite p–n homojunction. Top-view SEM images of (a) perovskite p–n homojunction and (b) perovskite p–n homojunction with the insert layer, inset: cross-sectional SEM images of corresponding samples. (c) XRD patterns of n-type perovskite film, n-type perovskite film covered with the PEA layer and p-type perovskite film on the PEA layer. (d and e) AFM topography images of the p-type perovskite film and p-type perovskite film deposited on the PEA layer. (f–g) KPFM images of the n-type and p-type perovskite films. (h–i) Potential profiles of the n-type and p-type perovskite films extracted from the selected linear area. (j) Secondary electron cut-off and (k) valence band of the n-type and p-type perovskite films deduced from helium I_α ($h\nu$ = 21.22 eV) UPS spectra. (l) Energy level alignment schematic of the as-prepared perovskite p–n homojunction structure.

can be inferred that n-type and p-type perovskite films were successfully fabricated. Additionally, the band gaps of these perovskite films were obtained from Tauc plots depicted in Fig. S8.† Accordingly, the energy level diagrams of the n- and p-type perovskite films were generated, as illustrated in Fig. 1l. The favorable alignment of energy levels of the n-type and p-type perovskite films can promote the extraction and transport of carriers, as demonstrated in Fig. 1l. This can help reduce the recombination of carriers within the perovskite absorption layer.

To estimate the effects of as-prepared perovskite p–n homojunction on carrier extraction and separation, we employed femtosecond transient absorption (fs-TAS), along with steady-state and time-resolved photoluminescence (PL) measurements to explore the carrier dynamics of perovskite samples on picosecond to nanosecond time scales. Three types of per-

ovskite samples: n-type perovskite (one perovskite film layer), p–n homojunction (n-type and p-type perovskite film stack), and the insert layer (n-type perovskite, PEA, and p-type perovskite film stack) were prepared for carrier dynamic characterization. All samples were subject to a 480 nm pump pulse with a pump energy of 2.2 μJ cm^{-2} during fs-TAS measurements to prevent multiple exciton generation. Fig. 2a displays the pseudo-color fs-TAS plots of different samples as a function of delay time and wavelength. The main photobleaching negative peak (PB) at ~780 nm for all samples was observed clearly, which is attributed to the state-filling of the carriers at the band edge.[45–47]

In Fig. 2b, the normalized TA spectra of the three types of perovskite samples, from 0.3 to 2 ps after excitation, are exhibited. The high-energy tail of the TA spectra gradually disappears over time, which is attributed to hot-carrier cooling processes.[48–50] The broader bleach signal of the n-type perovskite sample compared to p–n homojunction samples (with or without the insert layer) suggests that the p–n homojunction structure can rapidly separate/extract non-equilibrium carriers and thus accelerate the hot-carrier cooling process. The delay time of the non-equilibrium carrier is shown in Fig. S9.† The TA decay kinetics at 810 nm exhibited the same trend across all the three samples, as shown in Fig. 2c. The faster decrease of ΔA in the p–n homojunction samples (without and with the insert layer) than in the n-type perovskite sample indicates effective carrier separation/extraction in the perovskite p–n homojunction.

Fast charge separation/extraction in the p–n homojunction samples (without and with the insert layer) is further confirmed by steady-state and time-resolved PL spectra, as shown in Fig. 2d and e. Compared to the n-type perovskite, the steady-state PL peaks of the p–n homojunction samples (without and with the insert layer) show dramatic PL quenching, indicating that the p–n homojunction facilitates carrier separation and extraction. The time-resolved PL spectra

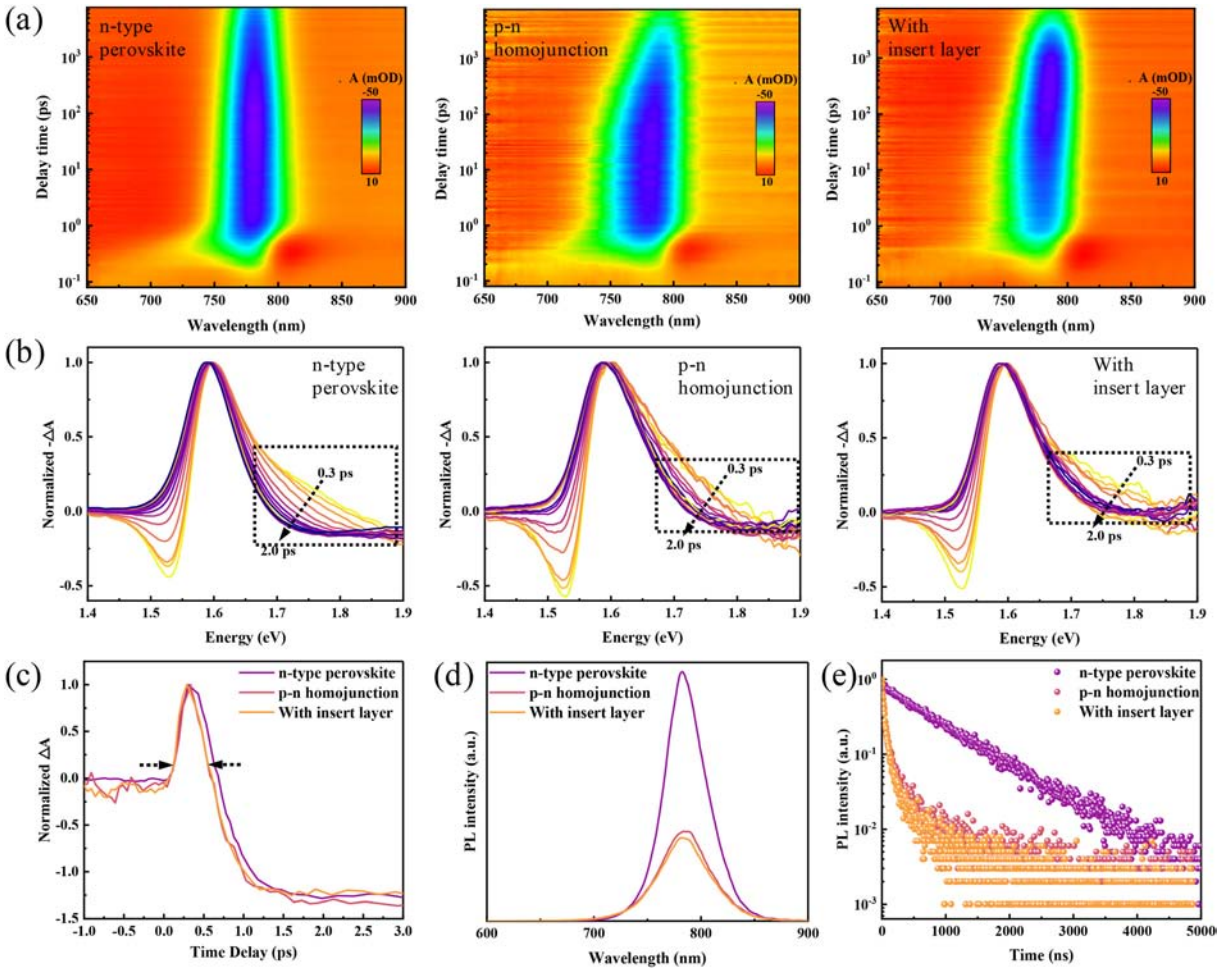

Fig. 2 Carrier dynamics of the single n-type perovskite film, perovskite p–n homojunction, and perovskite p–n homojunction with the insert layer. (a) Pseudo color plots and (b) high energy tails on the normalized bleaching spectra of three kinds of perovskite samples. (c) Ultrafast carrier dynamics of photoinduced absorption at 810 nm of the as-prepared perovskite samples. All TA results are obtained under 480 nm pump pulse with a pump energy of 2.2 μJ cm^{-2}. (d) Steady-state and (e) time-resolved PL spectra of the corresponding perovskite samples. Structures of the three kinds of samples are: FTO/n-type perovskite, FTO/n-type perovskite/p-type perovskite, FTO/n-type perovskite/PEA insert layer/p-type perovskite.

present that PL average lifetimes (τ_{ave}) of the n-type perovskite, p–n homojunction and p–n homojunction with the insert layer are estimated as 810.60, 142.45 and 139.69 ns, respectively, fitted by a bi-exponential model. The detailed parameters are summarized in Table S1 of ESI.† These results clearly illustrate that the p–n homojunction, with or without an insert layer, can enhance carrier separation/extraction in the perovskite layer and thereby suppress carrier recombination in devices.

To assess the inhibition effect of the PEA insert layer on ion diffusion between two perovskite layers, we doped the bottom perovskite film (n-type layer) with bromine (Br) ions and aged the perovskite homojunction with and without the insert layer for 120 hours under continuous illumination at various temperatures. Simultaneously, X-ray photoelectron spectroscopy (XPS) was used to track the content evolution of the Br element over time in the upper perovskite film (p-type layer) to determine if Br diffused from the bottom layer. For the perovskite homojunction without the insert layer (PHJ sample), as shown in Fig. 3a, it is apparent that with an increased aging temperature, the characteristic peak of Br is detected earlier, with a greater peak intensity. Conversely, for PHJ with the insert layer (with the insert layer sample), the signal of Br is weak, even under the aging conditions of 100 °C displayed in Fig. 3b. When the aging temperature increased to 60 °C, a visible Br characteristic peak at 68.3 eV was observed in the PHJ sample after 70 hours of aging, while for the PHJ with the insert layer sample, there exists no evident signal of Br. Increasing the temperature to 80 °C, the Br characteristic peak emerges even earlier in the PHJ sample after 40 hours of aging, with a more prominent peak intensity, while the PHJ with the insert layer sample still shows no observable peak. Then, with a further increase in aging temperature to 100 °C, a significant Br characteristic peak appears as early as 10 hours of aging in the PHJ sample, while a faint appearance of the Br characteristic peak is observed in the PHJ with the insert layer sample after aging for 100 hours. This indicates that even under severe conditions for a long time, the PEA insert layer can efficiently inhibit ion migration between the two perovskite films, which will greatly enhance the long-term operational stability of the perovskite homojunction. Fig. S10† substantiates this conclusion through X-ray photoelectron spectroscopy (XPS) depth profiling, which demonstrates the vertical distribution of Br elements along the film thickness in both PHJ films with and without the PEA insertion layer, before and after aging at a milder temperature of 60 °C for 120 hours. The outstanding inhibition effect of the PEA insert layer on the diffusion/migration of ions in PHJ is due to two reasons: one is the physical isolation between two perovskite layers and the other is molecular interactions between PEA and perovskite to lock halide ions through Pb═O and H–I bonds, which had been confirmed in our published study.[51] FTIR results shown in Fig. S11† further verify the molecular interactions between the PEA and perovskite.

To conduct a more intuitive comparison of the long-term thermal stability of the perovskite homojunction with and without the insert layer, digital photos and surface SEM images of these two samples at different aging times are exhibited in Fig. 3c–f. From Fig. 3c, the color of the perovskite film shifts from black to yellow with prolonged aging, indicating severe degradation. Morphological changes in the fresh and 120-hour aged film in Fig. 3d confirm this trend. In contrast, there is no obvious change in the color of the perovskite homojunction with the insert layer in Fig. 3e, and only slight alterations to the morphology of the film after 120 hours of aging are observed in Fig. 3f. These results suggest that the PHJ structure with the insert layer has better thermal stability than the control sample.

The thermal process is known to accelerate the movement of ions and promote ion diffusion between films, subsequently diminishing the structural integrity of perovskite films. Hence, the Urbach energy (E_u) calculated from the Tauc plots (shown in Fig. S12†) were adopted to qualify the changes of defect concentrations and structural disorder of PHJ with and without the insert layer during the thermal aging process. From Fig. 3g and h, it is clear that E_u values are primarily impacted by the aging temperature. When the temperature is below 80 °C, the E_u value of the control sample increases from 29.58 meV to 39.87 meV, while the perovskite homojunction with the insert layer increases from 29.46 meV to 37.76 meV after 120 hours of aging. Higher E_u values correspond to greater defect concentrations and higher structural disorders. When the aging temperature is increased to 100 °C, the control sample has an enormous increase in the E_u value, rising from 29.58 meV to 245.41 meV. Conversely, the increase in the E_u value of the perovskite homojunction with the insert layer is much smaller, rising from 29.46 meV to 147.24 meV. These results demonstrate that the insert layer can effectively suppress the increase of structural disorders and defect concentrations caused by thermal movement of ions. Accordingly, it can be concluded that the PEA insert layer can inhibit ion diffusion between the two perovskite layers, mitigate adverse effects induced by thermal movement of ions in the perovskite films, and thus increase the long-term stability of the PHJ.

The homojunction not only enhances carrier separation/extraction but also provides additional built-in potential (V_{bi}). Therefore, we conducted capacitance–voltage (C–V) measurements to determine the V_{bi} of the prepared perovskite samples. As shown in Fig. 4a, it is found that the V_{bi} values of the p–n homojunction and the homojunction with the insert layer are about 0.53 V and that of the single n-type perovskite is too small to observed. These results indicate that the as-prepared PHJ possesses a built-in potential of approximately 0.5 V, and the insert layer does not affect the V_{bi} value of the homojunction. Owing to its ability to enhance carrier separation/extraction, suppress carrier recombination, and provide an additional built-in potential, we anticipate a significant improvement in the performance of PHJ–PSCs. The J–V curves corresponding to the top efficiencies of PSCs assembled with the single n-type perovskite, perovskite p–n homojunction and homojunction with the insert layer are presented in Fig. 4b–d. These J–V characteristics were recorded during reverse and forward scans on devices having an effective area of 0.105 cm^2

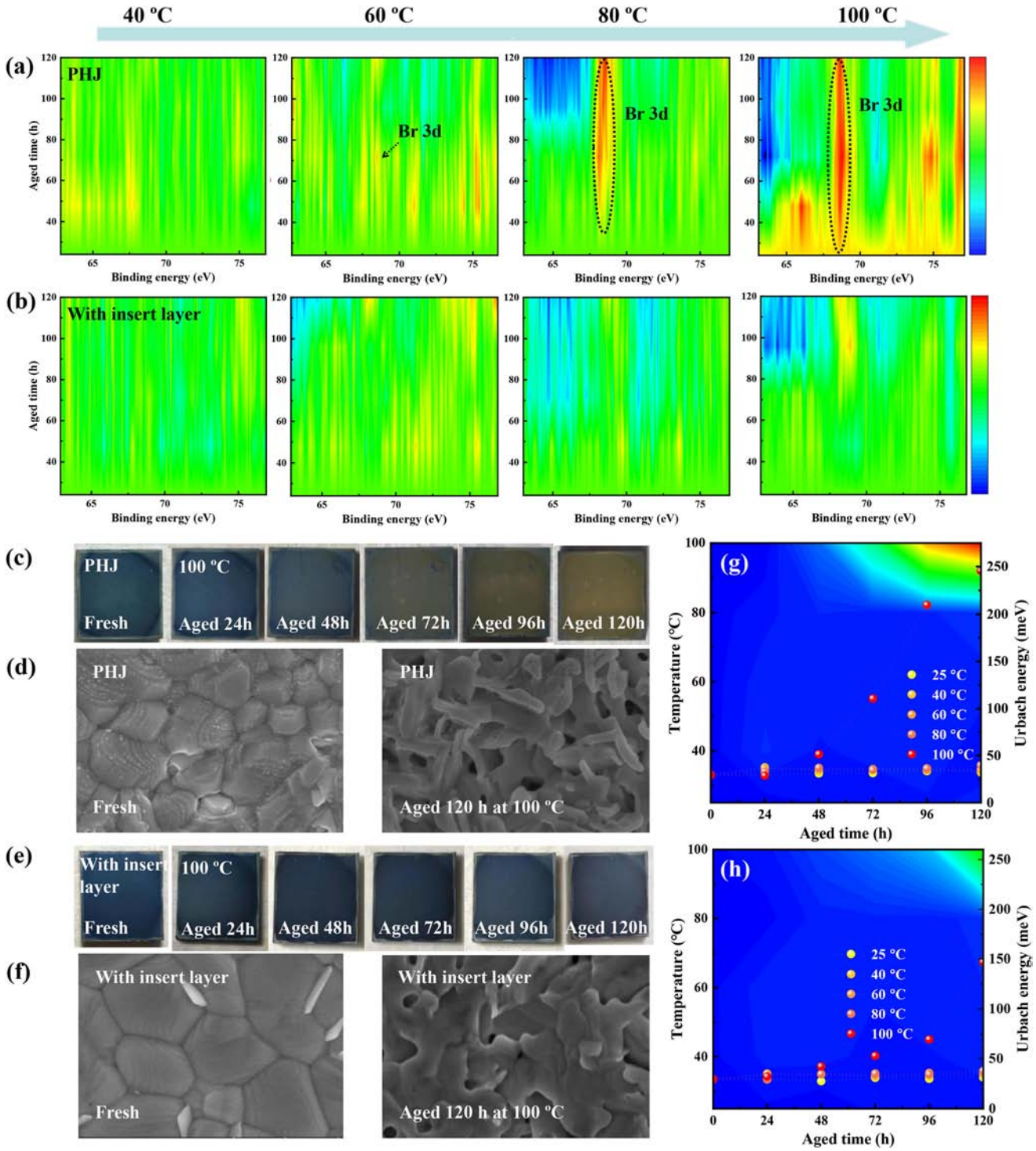

Fig. 3 Stabilization effect of the insert layer on the perovskite p–n homojunction. Evolution of Br 3d peaks (obtained from XPS Spectra) of the PHJ (a) without and (b) with insert layer. All tested samples were aged under continuous illumination at different temperatures. Photos of PHJ (c) without and (e) with insert layer during the aging process. Surface SEM images of corresponding samples (d) without and (f) with insert layer before and after aging. Changes of 2D maps of Urbach energy (E_u) of PHJ (g) without and (h) with the insert layer during aging process.

by employing a mask of 0.1 cm^2 in size. It is evident that the reverse-scan photoelectric conversion efficiency (PCE) of PHJ–PSCs (with or without the insert layer) exhibits a remarkable improvement compared to the traditional planar PSCs. The short-circuit current density (J_{SC}) increases from 24.24 to 26.06 mA cm^{-2}, and the open-circuit voltage (V_{OC}) increases from 1.11 to 1.13 V, resulting in an increase in PCE from 20.92% to 23.53%. Notably, the efficiency of the optimized

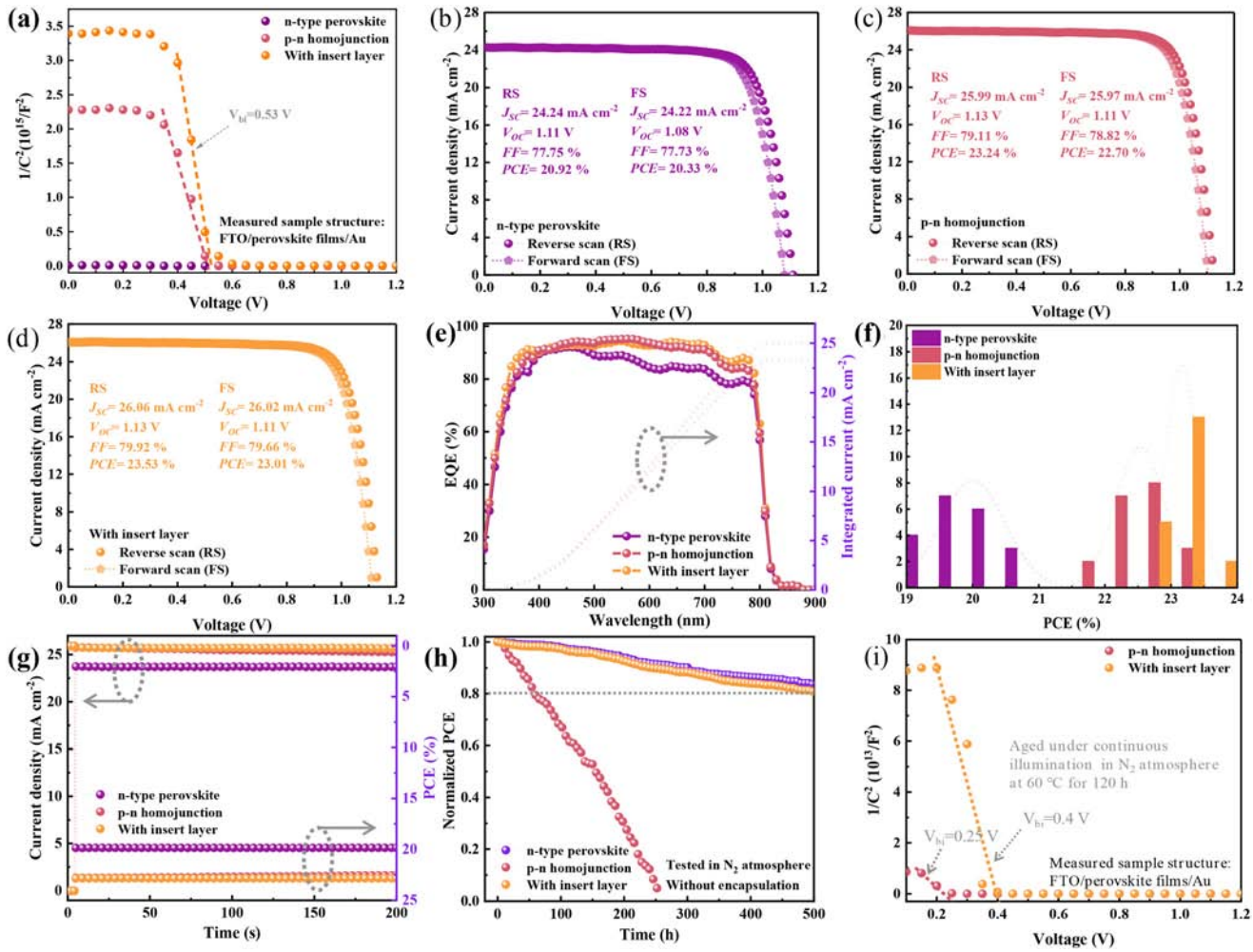

Fig. 4 Photovoltaic performance of PSCs. (a) Mott–Schottky plots of single n-type perovskite film, perovskite p–n homojunction and homojunction with the insert layer. (b–d) *J*–*V* curves of best-performing PSCs assembled by n-type perovskite film, perovskite p–n homojunction and homojunction with the insert layer. (e) EQE spectra and integrated photo current of the corresponding devices. (f) PCE distribution of PSCs assembled by n-type perovskite, p–n homojunction and homojunction with the insert layer. The data were from twenty individual devices. (g) Steady-state photo current density and power output at maximum power point of PHJ–PSCs without and with the insert layer. (h) MPP tracking of PHJ–PSCs without and with the insert layer according to the ISOS-L-1 protocol (1 Sun illumination without ultraviolet filter, ambient atmosphere, and inert atmosphere). (i) Mott–Schottky plots of PHJ without and with the insert layer after 120 h aging.

PHJ–PSC with the insert layer is comparable to that of the PHJ–PSC without the insert layer, indicating that the well-designed insert layer does not interfere with the function of the perovskite homojunction. The statistical distribution of the PCE values of PHJ–PSCs with various thicknesses of the insert layer are also presented in Fig. S13.† Fig. 4e displays external quantum efficiency (EQE) spectra and integrated current densities of optimized PSCs. The integrated current densities align well with J_{SC} values obtained from the *J*–*V* measurement, reaching 23.34, 25.05, and 25.07 mA cm^{-2}. The PCE distribution diagram shown in Fig. 4f indicates that the PHJ–PSCs with the insert layer have enhanced device reproducibility. Dark *J*–*V* curves of PHJ–PSCs without and with the insert layer are also provided in Fig. S14.† PHJ–PSC with the insert layer exhibited an obviously lower dark current than the control sample (PHJ–PSC), indicating the lower leakage current in devices with the insert layer.[52,53]

To validate the stability enhancement of PHJ–PSCs by the PEA insert layer, we conducted measurements of steady-state power output (SPO) at the maximum power point (MPP) under continuous light exposure and assessed the long-term operational stability (over 500 hours), as shown in Fig. 4g and h. The SPO measurement was performed in ambient air (relative humidity ~70%) at room temperature, while the long-term stability test was conducted in a nitrogen (N_2) atmosphere. The SPO efficiency of the homojunction PSC without the insert layer decreased from 22.82% to 22.56%, whereas the homojunction PSC with the insert layer and single n-type PSC exhibited no significant decrease, demonstrating a similar performance stability to the single n-type PSC (Fig. 4g). In the long-

term stability measurement (Fig. 4h), the normalized PCE of the PHJ–PSC without the insert layer experienced a drastic decrease after 200 hours of aging. In contrast, the PHJ–PSC with the insert layer demonstrated remarkable stability, indicating that it achieves a comparable level of stability to single-layer perovskite solar cells, maintaining an efficiency of over 80% of the original value after 500 hours of aging. To further understand the effect of V_{bi} changes of the p–n homojunction on the efficiency reduction of devices, we prepared samples with the structure of FTO/PHJ (without and with the insert layer)/Au and subjected them to continuous illumination at 60 °C in N_2 atmosphere for 120 hours. As shown in Fig. 4i, the V_{bi} value of samples without and with the insert layer are all decreased, and a serious decrease can be observed in the p–n homojunction sample (without insert layer), which decreased from 0.5 V to 0.25 V. This decrease is attributed to the diffusion and migration of ions between the two perovskite layers during the aging process, which can disrupt the homojunction structure and consequently reduce the V_{bi} values. Conversely, for the sample with insert layer, the V_{bi} value is decreased by about 0.1 V after 120 hours aging, highlighting the significant advantage of the insert layer in inhibiting the diffusion and migration of ions and enhancing the stability of the perovskite p–n homojunction.

3. Conclusion

In summary, we successfully constructed the PHJ with an insert layer by introducing ultrathin PEA film between the n-type and p-type perovskite films. This insert layer efficiently suppresses the diffusion and migration of ions between the perovskite films, greatly enhancing the long-term stability of PHJ and PHJ-based devices under continuous illumination and heating conditions. The optimized PHJ–PSCs without and with the insert layer achieved efficiencies of 23.53% and 23.24%, respectively, compared to the mere 20.92% efficiency of traditional planar PSCs. After 500 hours of continuous operation under one-sun illumination, the PHJ–PSC with the insert layer retained over 80% of its initial efficiency. This study demonstrates that the insert layer strategy can enhance the long-term operational stability of PHJ–PSCs and provides a pathway for fabricating more efficient and stable PSCs.

4. Experimental section

Materials

Titanium tetrachloride ($TiCl_4$), polyetheramine (PEA) and chlorobenzene (CB) were purchased from Innochem. *N*,*N*-Dimethylformamide (DMF), dimethyl sulfoxide (DMSO) and acetonitrile (ACN) were received from Acros Organics. Isopropanol (IPA) and lead iodide (PbI_2) were obtained from TCI Development Co., Ltd. Formamidine hydroiodate (FAI), methyl ammonium iodide (MAI) and methylammonium chloride (MACl) were provided by You Xuan Technology Co., Ltd. Later, 2,2,7,7-tetrakis(*N*,*N*-dip-methoxyphenylamine)9,9-spirobifluorene (Spiro-OMeTAD) and methyl ammonium bromide (MABr) were purchased from Polymer Light Technology Corp. Bis(trifluoromethane) sulfonimide lithium salt (Li–TFSI), 4-*tert*-butylpyridine (TBP), tris[2-((1*H*-pyrazol-1-yl)-4-*tert*-butylpyridine)cobalt(III)tris(bis(trifluoromethylsulfonyl) imide)] (FK209) were purchased from Sigma-Aldrich. All chemicals were used directly without further purification.

Device fabrication

FTO glasses (15 Ω sq^{-1}) were cleaned in the following order, in an ultrasonic bath for 20 min each, with DI–water, acetone, and ethanol. FTO substrates were treated with UV-ozone for 15 minutes before usage after being dried with high-purity nitrogen. For the ETL, chemical bath deposition was used to deposit TiO_2 layers on the FTO substrates. The FTO substrates were immersed in a $TiCl_4$/DI–water solution (v/v = 1 : 8) for 30 min at 70 °C. The FTO substrates were afterwards cleaned with water and ethanol, dried in air, and later given a 20-minute UV ozone treatment. Using a one-step anti-solvent technique, n-type perovskite films were created. A mixture of 2.1 M PbI_2, 1.16 M FAI, 0.63 M MAI, 0.14 M MABr, and 0.07 M MACl were dissolved in a DMF/DMSO mixed solvent (v/v = 9 : 1) to create the perovskite precursor solution. In a glove box, the precursor solution was agitated for 4 hours while remaining at room temperature. It was then filtered before use. Afterward, the perovskite precursor solution was spin-coated at 5000 rpm for 30 s; diethyl ether (1 mL) was poured onto the substrate at the start of spin coating for 10 s. The yellow transparent films were then transferred to a hot plate and annealed at 150 °C for 16 min to obtain the n-type perovskite films. The PEA insert layer was produced by spin-coating the PEA/IPA (v/v = 1 : 600) solution on the n-type perovskite at 5000 rpm for 30 s and later annealed at 100 °C for 1 min. For the p-type perovskite film, a 300 nm thick PbI_2 layer was prepared on the PEA insertion layer using vacuum evaporation at a deposition rate of 0.4 Å s^{-1}. Subsequently, a mixed solution containing FAI at 90 mg mL^{-1}, MACl at 9 mg mL^{-1}, and MABr at 9 mg mL^{-1} in IPA was spin-coated onto the PbI_2 film for 13 seconds at 5000 rpm. In XPS aging experiments, a different mixture with FAI at 90 mg mL^{-1} and MACl at 12 mg mL^{-1} dissolved in IPA was employed for spin-coating. After spin-coating, the sample underwent a pre-annealing step at 80 °C for 30 seconds, followed by annealing at 150° C for 16 minutes to yield the p-type perovskite film. For the HTL, the Spiro-OMeTAD solution was made by combining 76 mg of Spiro-OMeTAD, 30 μL of TBP, 23 μL of FK209 (300 mg mL^{-1} acetonitrile), and 20 μL of Li–TFSI (520 mg mL^{-1} acetonitrile) in 1 mL of chlorobenzene. The mixture was then agitated for 12 hours at room temperature. After that, a hole transport layer was created by spin-coating the Spiro-OMeTAD solution onto the p-type perovskite film for 20 s at 4500 rpm. Finally, using vacuum evaporation technological devices, 100 nm thick Au electrodes were formed at a pressure of 10^{-4} Torr. (Kurt J. Lesker).

Characterization

After spectral correction, photocurrent density–voltage (*J–V*) curves were measured using the IVS-KA5000 measuring software and a digital source meter (Keithley 2400) under AM 1.5 simulated sunshine (100 $mWcm^{-2}$) from a solar simulator (Enlitech Technology Co., Ltd). A HITACHI Regulus SU8010 scanning electron microscope was utilized to assess the morphology of the perovskite films. Steady-state photoluminescence (PL) spectra were measured using a fluorescence spectrometer (Edinburgh FLS1000). XPS (UPS) testing was performed on an ESCALAB Xi+ (Thermo Fisher) instrument. The absorption spectra of perovskite films were obtained by a UV spectrophotometer (UV-2450). The static contact angle of the perovskite films was obtained by a contact angle meter (OCA15EC). The chemical compositions and structures of the perovskite films were analysed by X-ray diffraction (Rigaku Ultima IV X-ray diffractometer, Cu-Kα radiation λ = 0.15406 nm). The surface AFM and KPFM were carried out by a Dimension Icon SPM (Bruker). FTIR testing was performed with a Nicolet IS50 (Thermo Fisher) instrument.

Conflicts of interest

The authors declare no conflict of interest.

Acknowledgements

This work is supported partially by the National Natural Science Foundation of China (Grant No. 52002070, 52232008, 51972110, 52102245, and 52072121), Natural Science Foundation project of Fujian Province (No. 2020J01197), Educational Research Project of Young and Middle-Aged Teachers in Fujian Province (JAT190072), Natural Science Foundation of Gansu Province (Grant No. 20JR5RA197), Beijing Natural Science Foundation (2222076 and 2222077), Beijing Science and Technology Project (Z211100004621010), 2022 Strategic Research Key Project of Science and Technology Commission of the Ministry of Education, Huaneng Group Headquarters Science and Technology Project (HNKJ20-H88), Fundamental Research Funds for the Central Universities (2022MS029, 2022MS02, and 2022MS031) and NCEPU "Double First-Class" Program.

References

1 Y. Zhao, F. Ma, Z. Qu, S. Yu, T. Shen, H.-X. Deng, X. Chu, X. Peng, Y. Yuan, X. Zhang and J. You, *Science*, 2022, **377**, 531–534.
2 R. Lin, J. Xu, M. Wei, Y. Wang, Z. Qin, Z. Liu, J. Wu, K. Xiao, B. Chen, S. M. Park, G. Chen, H. R. Atapattu, K. R. Graham, J. Xu, J. Zhu, L. Li, C. Zhang, E. H. Sargent and H. Tan, *Nature*, 2022, **603**, 73–78.
3 C. Wang, Y. Zhao, T. Ma, Y. An, R. He, J. Zhu, C. Chen, S. Ren, F. Fu, D. Zhao and X. Li, *Nat. Energy*, 2022, **7**, 744–753.
4 S. Qin, C. Lu, Z. Jia, Y. Wang, S. Li, W. Lai, P. Shi, R. Wang, C. Zhu, J. Du, J. Zhang, L. Meng and Y. Li, *Adv. Mater.*, 2022, **34**, e2108829.
5 L. Luo, H. Zeng, Z. Wang, M. Li, S. You, B. Chen, A. Maxwell, Q. An, L. Cui, D. Luo, J. Hu, S. Li, X. Cai, W. Li, L. Li, R. Guo, R. Huang, W. Liang, Z.-H. Lu, L. Mai, Y. Rong, E. H. Sargent and X. Li, *Nat. Energy*, 2023, **8**, 294–303.
6 F. Li, X. Deng, Z. Shi, S. Wu, Z. Zeng, D. Wang, Y. Li, F. Qi, Z. Zhang, Z. Yang, S.-H. Jang, F. R. Lin, S. W. Tsang, X.-K. Chen and A. K. Y. Jen, *Nat. Photonics*, 2023, **17**, 478–484.
7 J. Park, J. Kim, H.-S. Yun, M. J. Paik, E. Noh, H. J. Mun, M. G. Kim, T. J. Shin and S. I. Seok, *Nature*, 2023, **616**, 724–730.
8 W. Zhao, H. Lin, Y. Li, D. Wang, J. Wang, Z. Liu, N. Yuan, J. Ding, Q. Wang and S. Liu, *Adv. Funct. Mater.*, 2022, **32**, 2112032.
9 P. Zhu, S. Gu, X. Luo, Y. Gao, S. Li, J. Zhu and H. Tan, *Adv. Energy Mater.*, 2020, **10**, 1903083.
10 Z. Zhang, Y. Gao, Z. Li, L. Qiao, Q. Xiong, L. Deng, Z. Zhang, R. Long, Q. Zhou, Y. Du, Z. Lan, Y. Zhao, C. Li, K. Müllen and P. Gao, *Adv. Mater.*, 2021, **33**, 2008405.
11 J. Zhang, J. Yang, R. Dai, W. Sheng, Y. Su, Y. Zhong, X. Li, L. Tan and Y. Chen, *Adv. Energy Mater.*, 2022, **12**, 2103674.
12 Z. Xiong, X. Chen, B. Zhang, G. O. Odunmbaku, Z. Ou, B. Guo, K. Yang, Z. Kan, S. Lu, S. Chen, N. A. N. Ouedraogo, Y. Cho, C. Yang, J. Chen and K. Sun, *Adv. Mater.*, 2022, **34**, 2106118.
13 L. McGovern, M. H. Futscher, L. A. Muscarella and B. Ehrler, *J. Phys. Chem. Lett.*, 2020, **11**, 7127–7132.
14 H. Li, C. Zhang, C. Gong, D. Zhang, H. Zhang, Q. Zhuang, X. Yu, S. Gong, X. Chen, J. Yang, X. Li, R. Li, J. Li, J. Zhou, H. Yang, Q. Lin, J. Chu, M. Grätzel, J. Chen and Z. Zang, *Nat. Energy*, 2023, **8**, 946–955.
15 S. You, F. T. Eickemeyer, J. Gao, J.-H. Yum, X. Zheng, D. Ren, M. Xia, R. Guo, Y. Rong, S. M. Zakeeruddin, K. Sivula, J. Tang, Z. Shen, X. Li and M. Grätzel, *Nat. Energy*, 2023, **8**, 515–525.
16 B. Li, X. Wu, H. Zhang, S. Zhang, Z. Li, D. Gao, C. Zhang, M. Chen, S. Xiao, A. K.-Y. Jen, S. Yang and Z. Zhu, *Adv. Funct. Mater.*, 2022, **32**, 2205870.
17 B. Liu, X. Ren, R. Li, Y. Chen, D. He, Y. Li, Q. Zhou, D. Ma, X. Han and X. Shai, *Adv. Mater.*, 2024, 2312679.
18 Y. Zhu, Z. Zhang, X. Zhao, M. Li, Y. Feng, S. Zhang, W. Gao, J. Chen, J. X. Tang and C. Chen, *Adv. Energy Mater.*, 2024, 2303946.
19 B. Liu, Q. Zhou, Y. Li, Y. Chen, D. He, D. Ma, X. Han, R. Li, K. Yang and Y. Yang, *Angew. Chem., Int. Ed.*, 2024, **63**, e202317185.
20 Q. Zhou, B. Liu, Y. Chen, D. Ma, X. Han, D. He, Z. Zhang, H. Yang, L. Ding and J. Feng, *Adv. Funct. Mater.*, 2024, 2315064.

21 Y.-N. Lu, J.-X. Zhong, Y. Yu, X. Chen, C.-Y. Yao, C. Zhang, M. Yang, W. Feng, Y. Jiang, Y. Tan, L. Gong, X. Wei, Y. Zhou, L. Wang and W.-Q. Wu, *Energy Environ. Sci.*, 2021, **14**, 4048–4058.

22 S. Xiong, Z. Hou, S. Zou, X. Lu, J. Yang, T. Hao, Z. Zhou, J. Xu, Y. Zeng, W. Xiao, W. Dong, D. Li, X. Wang, Z. Hu, L. Sun, Y. Wu, X. Liu, L. Ding, Z. Sun, M. Fahlman and Q. Bao, *Joule*, 2021, **5**, 467–480.

23 B. Liu, Y. Wang, Y. Wu, Y. Zhang, J. Lyu, Z. Liu, S. Bian, X. Bai, L. Xu, D. Zhou, B. Dong and H. Song, *Adv. Energy Mater.*, 2023, **13**, 2203352.

24 Z. Yang, Z. Yu, H. Wei, X. Xiao, Z. Ni, B. Chen, Y. Deng, S. N. Habisreutinger, X. Chen, K. Wang, J. Zhao, P. N. Rudd, J. J. Berry, M. C. Beard and J. Huang, *Nat. Commun.*, 2019, **10**, 4498.

25 K. Xiao, R. Lin, Q. Han, Y. Hou, Z. Qin, H. T. Nguyen, J. Wen, M. Wei, V. Yeddu, M. I. Saidaminov, Y. Gao, X. Luo, Y. Wang, H. Gao, C. Zhang, J. Xu, J. Zhu, E. H. Sargent and H. Tan, *Nat. Energy*, 2020, **5**, 870–880.

26 J. Zhang, Y. Sun, C. Huang, B. Yu and H. Yu, *Adv. Energy Mater.*, 2022, **12**, 2202542.

27 C. Chen, Z. Song, C. Xiao, D. Zhao, N. Shrestha, C. Li, G. Yang, F. Yao, X. Zheng, R. J. Ellingson, C.-S. Jiang, M. Al-Jassim, K. Zhu, G. Fang and Y. Yan, *Nano Energy*, 2019, **61**, 141–147.

28 W.-J. Yin, T. Shi and Y. Yan, *Appl. Phys. Lett.*, 2014, **104**, 063903.

29 B. Dänekamp, C. Müller, M. Sendner, P. P. Boix, M. Sessolo, R. Lovrincic and H. J. Bolink, *J. Phys. Chem. Lett.*, 2018, **9**, 2770–2775.

30 Y. Zhang, Z. Yang, T. Ma, Z. Ai, C. Wang and X. Li, *Adv. Energy Mater.*, 2023, **13**, 2203366.

31 P. Cui, D. Wei, J. Ji, H. Huang, E. Jia, S. Dou, T. Wang, W. Wang and M. Li, *Nat. Energy*, 2019, **4**, 150–159.

32 J. Ji, L. Yan, X. Wang, S. Du, B. Liu, H. Huang, S. Qu, P. Cui, Y. Li and M. Li, *Sol. RRL*, 2022, **6**, 2200028.

33 S. Wu, R. Chen, S. Zhang, B. H. Babu, Y. Yue, H. Zhu, Z. Yang, C. Chen, W. Chen, Y. Huang, S. Fang, T. Liu, L. Han and W. Chen, *Nat. Commun.*, 2019, **10**, 1161.

34 J. Yang, S. Xiong, T. Qu, Y. Zhang, X. He, X. Guo, Q. Zhao, S. Braun, J. Chen, J. Xu, Y. Li, X. Liu, C. Duan, J. Tang, M. Fahlman and Q. Bao, *ACS Appl. Mater. Interfaces*, 2019, **11**, 13491–13498.

35 E. H. Jung, N. J. Jeon, E. Y. Park, C. S. Moon, T. J. Shin, T.-Y. Yang, J. H. Noh and J. Seo, *Nature*, 2019, **567**, 511–515.

36 J. Wang, P. Zhao, Y. Hu, Z. Lin, J. Su, J. Zhang, J. Chang and Y. Hao, *Sol. RRL*, 2021, **5**, 2100121.

37 Q. Wang, Y. Shao, H. Xie, L. Lyu, X. Liu, Y. Gao and J. Huang, *Appl. Phys. Lett.*, 2014, 105.

38 B. Dänekamp, C. Müller, M. Sendner, P. P. Boix, M. Sessolo, R. Lovrincic and H. J. Bolink, *J. Phys. Chem. Lett.*, 2018, **9**, 2770–2775.

39 M. Hu, C. Bi, Y. Yuan, Y. Bai and J. Huang, *Adv. Sci.*, 2016, **3**, 1500301.

40 C. Bi, Q. Wang, Y. Shao, Y. Yuan, Z. Xiao and J. Huang, *Nat. Commun.*, 2015, **6**, 7747.

41 C. Liu, Y. B. Cheng and Z. Ge, *Chem. Soc. Rev.*, 2020, **49**, 1653–1687.

42 C. Xu, X. Chen, S. Ma, M. Shi, S. Zhang, Z. Xiong, W. Fan, H. Si, H. Wu, Z. Zhang, Q. Liao, W. Yin, Z. Kang and Y. Zhang, *Adv. Mater.*, 2022, **34**, e2109998.

43 Y. Luo, K. Liu, L. Yang, W. Feng, L. Zheng, L. Shen, Y. Jin, Z. Fang, P. Song, W. Tian, P. Xu, Y. Li, C. Tian, L. Xie and Z. Wei, *Nat. Commun.*, 2023, **14**, 3738.

44 Y. Wang, L. Li, Z. Wu, R. Zhang, J. Hong, J. Zhang, H. Rao, Z. Pan and X. Zhong, *Angew. Chem., Int. Ed.*, 2023, **62**, e202302342.

45 M. Singh, I. H. Ho, A. Singh, C.-W. Chan, J.-W. Yang, T.-F. Guo, H. Ahn, V. Tung, C. W. Chu and Y.-J. Lu, *ACS Photonics*, 2022, **9**, 3584–3591.

46 T. C. Sum, N. Mathews, G. Xing, S. S. Lim, W. K. Chong, D. Giovanni and H. A. Dewi, *Acc. Chem. Res.*, 2016, **49**, 294–302.

47 Q. Wei, J. Yin, O. M. Bakr, Z. Wang, C. Wang, O. F. Mohammed, M. Li and G. Xing, *Angew. Chem., Int. Ed.*, 2021, **60**, 10957–10963.

48 X. Wang, D. Huo, X. Wang, M. Li, Y. Wang and Y. Wan, *J. Phys. Chem. Lett.*, 2021, **12**, 6907–6913.

49 F. Zhang, S. Ye, H. Zhang, F. Zhou, Y. Hao, H. Cai, J. Song and J. Qu, *Nano Energy*, 2021, **89**, 106370.

50 Q. Guo, Z. Dai, C. Dong, Y. Ding, N. Jiang, Z. Wang, L. Gao, C. Duan, Q. Guo and E. Zhou, *Chem. Eng. J.*, 2023, **461**, 142025.

51 Q. Cai, Y. Yao, Y. Lu, M. Wang, Y. Zhang, D. Song, Z. Xu, X. Li and D. Wei, *Phys. Chem. Chem. Phys.*, 2023, **25**, 6955–6962.

52 L. Yang, H. Zhou, Y. Duan, M. Wu, K. He, Y. Li, D. Xu, H. Zou, S. Yang, Z. Fang, S. Liu and Z. Liu, *Adv. Mater.*, 2023, **35**, 2211545.

53 Y. Li, X. Lu, Y. Mei, C. Dong, D. T. Gangadharan, K. Liu, Z. Wang, S. Qu, M. I. Saidaminov, W. Zhang and F. Tan, *Adv. Funct. Mater.*, 2023, **33**, 2301920.